Materials Advances

ROYAL SOCIETY OF CHEMISTRY

PAPER

View Article Online
View Journal | View Issue

Cite this: *Mater. Adv.*, 2023, 4, 1572

The giant tunneling electroresistance effect in monolayer In_2SSeTe-based lateral ferroelectric tunnel junctions†

Zhou Cui,[a] Ting Li,[a] Rui Xiong,[a] Cuilian Wen,*[a] Yinggan Zhang,[b] Jingying Zheng,[a] Bo Wu[a] and Baisheng Sa*[a]

Received 13th December 2022,
Accepted 29th January 2023

DOI: 10.1039/d2ma01079h

rsc.li/materials-advances

Two-dimensional (2D) asymmetric Janus materials display in-plane and out-of-plane intrinsic ferroelectricity due to their asymmetrical structures, which makes them suitable for ferroelectric data storage devices. Herein, by performing density functional calculations combined with nonequilibrium Green function simulations, we systematically study the ferroelectric properties of the 2D Janus In_2SSeTe monolayer and the electronic transport properties of the related ferroelectric tunnel junctions (FTJs) by employing graphene/germanene as the electrode. It is highlighted that both ferroelectric states of graphene/In_2SSeTe heterostructures show Ohmic contact, which is beneficial for decreasing the power dissipation of devices. Furthermore, the tunneling electroresistance (TER) ratios of the In_2SSeTe-based FTJs increase with the length of the devices. Interestingly, the FTJs of 9 nm central scattering region length with graphene/In_2SSeTe and germanene/In_2SSeTe electrodes can achieve maximum TER ratios of 2.24×10^7% and 2.98×10^8%, respectively. We believe that our findings will shed light on the design and application of the In_2SSeTe monolayer in FTJ devices.

Introduction

Ferroelectric tunnel junctions (FTJs), composed of two metallic electrodes separated by a thin ferroelectric material, have attracted global attention due to their potential applications in nonvolatile memory devices.[1–4] The spontaneous polarization of ferroelectric materials can be switched by an external electrical field, which results in the tunneling electroresistance (TER) effect in FTJs.[5–7] In the early years, FTJs with thin films of three-dimensional (3D) ferroelectric materials were employed as tunnel barriers.[8,9] Conventional 3D ferroelectric materials prefer perovskite structures, such as $BaTiO_3$ and $PbTiO_4$.[10,11] Up to now, a number of strategies have been put forward to achieve considerable TER ratios in conventional 3D FTJs. For example, a TER ratio of 400% at room temperature can be achieved in the $BaTiO_3$-based FTJ by reducing the $BaTiO_3$ layer thickness to two unit cells (~0.8 nm).[12] By introducing Na (or Li) substitutions for Ti atoms at the right interface of Pt/$BaTiO_3$/Pt ferroelectric tunnel junctions, a TER ratio up to 10^5% is achieved based on density-functional-theory calculations.[13] Recently, by engineering the Schottky barrier at the Nb:$SrTiO_3$ interface, an optimum TER ratio of 6×10^6 has been realized in Pt/$BaTiO_3$/Nb:$SrTiO_3$ FTJs.[14] However, stability and reproducibility at room temperature are intractable obstacles to these conventional 3D FTJs, with the ever-growing commercial requirements of low-power and high-speed in nanoscale nonvolatile memory devices.[15,16] Besides, with the ferroelectric material reduced to the nanoscale size, the inhibiting effect of the depolarization field on the ferroelectric properties is more apparent.[17] More importantly, the electronic coupling between the ferroelectric and electrode materials is greatly destroyed due to the dangling bonds and defects at the interface.[18] Therefore, new ferroelectric materials that can eliminate the above problems are greatly sought after for developing high-performance FTJs.

The successful synthesis of graphene opened an emerging horizon to develop artificial two-dimensional (2D) materials.[19] 2D materials show a lot of advantages in practical applications, such as ultrathin atomic thickness, smooth surfaces and the absence of dangling bonds on the surface.[20–22] Therefore, it is of interest to answer the question if 2D ferroelectric materials are good choices for overcoming the inherent disadvantages of 3D FTJs. A significant number of 2D ferroelectric materials, such as $CuInP_2S_6$,[23–25] α-In_2Se_3[26,27] and MX (M = Sn, Ge;

[a] *Multiscale Computational Materials Facility, and Key Laboratory of Eco-materials Advanced Technology, College of Materials Science and Engineering, Fuzhou University, Fuzhou 350100, P. R. China. E-mail: clwen@fzu.edu.cn, bssa@fzu.edu.cn*

[b] *College of Materials, Fujian Provincial Key Laboratory of Theoretical and Computational Chemistry, Xiamen University, Xiamen 361005, P. R. China*

† Electronic supplementary information (ESI) available. See DOI: https://doi.org/10.1039/d2ma01079h

X = S, Se),[28,29] have been prompted to possess in-plane or out-of-plane spontaneous polarization theoretically and experimentally. For instance, 2D $CuInP_2S_6$ is confirmed in the experiment to exhibit room temperature ferroelectricity with a transition temperature of ~320 K, and the $CuInP_2S_6$/Si ferroelectric heterostructure has been demonstrated to exhibit good memory performance with an on/off ratio of ~100.[24] Layered α-In_2Se_3 is predicted to maintain room-temperature out-of-plane polarized ferroelectric behavior with the thickness down to a single layer limit.[26] Recently, the out-of-plane ferroelectricity in van der Waals layered α-In_2Se_3 nanoflakes has been demonstrated experimentally.[27] Furthermore, some high-performance FTJs with 2D ferroelectric materials have been predicted in recent years.[30] A lateral FTJ based on the In- and Sb-doped SnSe monolayer with a large TER of 1460% has been proposed.[31] Moreover, a giant TER ratio as high as 10^4% is realized in ferroelectric tunnel junctions with top contact between Au(010) and In_2Se_3.[32] The recent theoretical studies on a lateral 2D FTJ constructed by graphene and ferroelectric α-In_2Se_3 achieved an excellent TER ratio of ~1×10^8%, suggesting its potential for ferroelectric memory devices.[33] Nevertheless, the study of integrating ferroelectrics into devices is still in its infancy, and it is urgent to search for new 2D ferroelectric materials with distinguished device performance.

Among various 2D materials, asymmetric Janus 2D materials has caught a lot of attention because they display different fascinating characteristics on two opposite surfaces.[34,35] Janus MXY (M =Mo or W, X/Y = S, Se, or Te) monolayers show distinguished out-of-plane piezoelectric polarization, which reveals their potential applications in actuators, sensors and surface acoustic waves.[36] Besides, Janus In_2X_2Y (X/Y = S, Se, and Te) monolayers are predicted to be desirable in the overall water splitting and piezoelectric devices.[37] It is worth noting that Janus 2D materials display in-plane and out-of-plane intrinsic piezoelectricity and ferroelectricity, due to their asymmetric structures.[38] On the other hand, due to the outstanding transport properties of the Dirac fermions in graphene layers, graphene-based heterostructures show a conceptually new degree of flexibility in the design of materials and devices.[39–41] 2D Dirac semimetals, like graphene and germanene, are promising atomically thin electrodes in designing novel devices.[42,43] Therefore, a systematical understanding of the corresponding Janus monolayer as well as the corresponding 2D Dirac semimetal heterostructures for application in FTJs is of great interest and importance.

Herein, inspired by the unique features of α-In_2Se_3 and the related Janus In_2X_2Y (X/Y = S, Se, and Te) monolayers,[44] which have excellent prospects for applications in multifunctional energy conversion, we construct a 2D Janus In_2SSeTe monolayer by replacing two different elements on the surfaces of the α-In_2S_3 monolayer to investigate the potential application in ferroelectric data storage devices. The phonon dispersion curves and AIMD simulations demonstrated the stability of two ferroelectric states of the In_2SSeTe monolayer. Furthermore, the tunneling electroresistance performances of the two types of FTJs are investigated using graphene/In_2SSeTe or germanene/In_2SSeTe electrodes. Meanwhile, the FTJs with different central scattering region lengths are considered to investigate the tunneling electroresistance performance *versus* the central scattering region lengths. Large TER ratios have been achieved in graphene and germanene-based FTJs, which verifies their great potential application in ferroelectric data storage devices.

Computational details

The different stacking configurations for In_2SSeTe/graphene and In_2SSeTe/germanene heterostructures were built using the ALKEMIE platform.[45,46] Based on the density functional theory (DFT) calculations, the structural relaxations were implemented in the Vienna *ab initio* Simulation Package (VASP).[47] The generalized gradient approximation (GGA) with the Perdew–Burk–Ernzerhof (PBE)[48] functional was adopted for the exchange and correlation potentials. The plane-wave cutoff energy was set to 500 eV, and $14 \times 14 \times 1$ and $9 \times 9 \times 1$ *k*-points were utilized for the optimization and self-consistent calculations of monolayers and heterostructures. The van der Waals interaction was described by the DFT-D3 method.[49,50] The vacuum thickness was set to 20 Å to avoid interlayer interaction. The convergence energies for electrons and forces for atoms were 1×10^{-6} eV and 0.01 eV Å^{-1}, respectively. The PHONOPY code[51] was employed to study the lattice dynamic stabilities of monolayers. Besides, *ab initio* molecular dynamics (AIMD) simulations[52,53] were performed to understand the thermodynamic stability of monolayers and heterostructures. The dipole correction[54] was taken into consideration. The Heyd–Scuseria–Ernzerhof (HSE06)[55] hybrid density functional was employed for the calculation of electronic structures to get precise band gaps. The nudged elastic band (NEB)[56,57] method was employed to determine the energy barriers of the kinetic processes from $P_\uparrow$ to $P_\downarrow$ of monolayers and heterostructures.

The quantum transport calculations based on the non-equilibrium Green's function (NEGF)[58] of the FTJs were performed using the QuantumWise Atomistix Toolkit (QuantumATK) Q-2021.06 package.[59] The GGA-PBE functional with a linear combination of atomic orbitals (LCAO) norm-conserving PseudoDojo pseudopotential[60] was employed. The double-zeta basis set was employed to expand wave functions.[61] The plane-wave cutoff of 105 Hartree was employed. The convergence criterion of the force was 0.01 eV Å^{-1}. The $7 \times 1 \times 128$ and $7 \times 1 \times 1$ Monkhorst *k*-point meshes were utilized for the self-consistent calculation of the electrodes and central scattering regions for the transport calculations, and the denser 121×1 Monkhorst-point meshes were used for the transport calculations. The tunneling conductance as a function of electron energy E is defined as[62]

$$G(E) = \frac{2e^2}{h} T(E) \quad (1)$$

where $T(E) = \sum_{k_\parallel} T(k_\parallel, E)$ is the *k*-point averaged transmission function at energy E, and $T(k_\parallel,E)$ is the *k*-resolved transmission

function with $k_{\parallel} = k_x$. The tunnel electroresistance (TER) ratio is calculated by the formula[63]

$$\mathrm{TER} = \frac{|G_{\uparrow} - G_{\downarrow}|}{\min(G_{\uparrow}, G_{\downarrow})} \quad (2)$$

where $G_{\uparrow}$ and $G_{\downarrow}$ are the tunneling conductances of the FTJs when the In_2SSeTe ferroelectric layer is in the up-polarized ($P_{\uparrow}$) state and the down-polarized ($P_{\downarrow}$) state, respectively.

Results and discussion

The In_2SSeTe monolayers were obtained by replacing S atoms on the surface terminations with Se and Te atoms in the ferroelectric α-In_2S_3 monolayer. Fig. 1(a) and (b) show the structures of two different ferroelectric states of the proposed In_2SSeTe monolayers, for which S atoms sitting right across the lower and upper In atoms are named as In_2SSeTe-$P_{\downarrow}$ and In_2SSeTe-$P_{\uparrow}$, respectively. The optimized lattice constants for In_2SSeTe-$P_{\downarrow}$ and In_2SSeTe-$P_{\uparrow}$ are 4.183 and 4.179 Å, respectively. To check the stability of the proposed In_2SSeTe monolayers, the phonon calculations and AIMD simulations were performed, as shown in Fig. S1 (ESI†). Minor imaginary frequencies at Γ points are observed from the phonon dispersion curves. Such minor imaginary frequency could be eliminated by using larger supercells or applying small strain,[64,65] revealing that In_2SSeTe-$P_{\downarrow}$ and In_2SSeTe-$P_{\uparrow}$ are stable from the lattice dynamic point of view. Besides, after annealing the In_2SSeTe monolayer for 9 ps at 300 K in AIMD simulations, the total energies of In_2SSeTe-$P_{\uparrow}$ and In_2SSeTe-$P_{\downarrow}$ are limited in a narrow window. Also, no significant distortion can be found in the final structures, demonstrating their thermal stabilities.[66] Therefore, both the phonon calculations and AIMD simulations confirm the stabilities of In_2SSeTe-$P_{\downarrow}$ and In_2SSeTe-$P_{\uparrow}$, which might verify their feasibility in the experiment. Furthermore, we unravel the electronic structures of the proposed In_2SSeTe monolayers. The band structures of In_2SSeTe-$P_{\downarrow}$ and In_2SSeTe-$P_{\uparrow}$ using the HSE06 method are exhibited in Fig. 1(c) and (d), respectively. Both ferroelectric states of In_2SSeTe show semiconducting electronic structure features. Herein, In_2SSeTe-$P_{\downarrow}$ holds an indirect band gap, in which its conduction band minimum (CBM) is located at the Γ point, and its valence band maximum (VBM) is located between Γ and M points. On the other hand, In_2SSeTe-$P_{\uparrow}$ has a direct band gap, where both the CBM and VBM are located at the Γ point. Interestingly, the predicted band gaps for In_2SSeTe-$P_{\downarrow}$ and In_2SSeTe-$P_{\uparrow}$ are 2.20 and 0.25 eV, respectively. The significant difference of band gaps will lead to different electron transmission capacities in the application of FTJ devices. It is worth noting that an appropriate electric field could induce the transition between In_2SSeTe-$P_{\downarrow}$ and In_2SSeTe-$P_{\uparrow}$, similar to In_2X_3 (X = S, Se, Te).[67] Therefore, In_2SSeTe is a promising candidate for ferroelectric switching devices.

Graphene and germanene possess hexagonal honeycomb structures (see Fig. S2(a) and (b), ESI†) with lattice constants of 2.46 Å and 4.06 Å, respectively. The $\sqrt{3} \times \sqrt{3}$ graphene and 1 × 1 germanene unit cells show small lattice mismatches of 1.86% and 2.94% with the $P_{\downarrow}$ state of the In_2SSeTe monolayer. The calculated band structures shown in Fig. S2(c) and (d) (ESI†) reveal their linearly dispersing electronic bands at the Fermi level, indicating the intrinsic high carrier mobility of the Dirac fermions in graphene and germanene.[68] Herein, we construct the lateral FTJs by employing graphene/In_2SSeTe and germanene/In_2SSeTe heterostructures as the electrodes. Before building the ferroelectric tunnel junctions (FTJs), In_2SSeTe with the $P_{\downarrow}$ state regarded as the initial state was employed to construct the heterostructures with graphene or germanene to get the most favorable stacking configurations. For graphene/In_2SSeTe-$P_{\downarrow}$ heterostructures, there are three types of stacking configurations, *i.e.*, the atoms of In_2SSeTe-$P_{\downarrow}$ located above either the centers of the hexagons, bonds, or C atoms. As depicted in Fig. 2, six different stacking configurations of graphene/In_2SSeTe-$P_{\downarrow}$ heterostructures are considered due to two different termination surfaces (*i.e.*, Se and Te terminated surfaces) of In_2SSeTe-$P_{\downarrow}$. On the

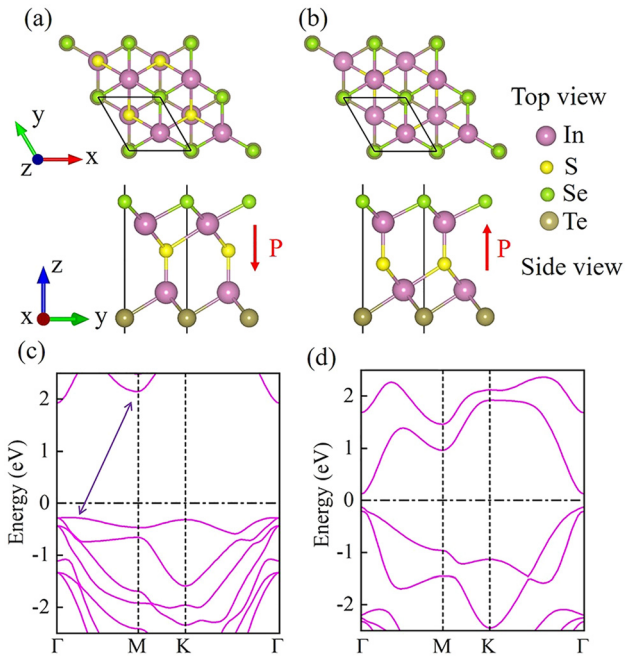

Fig. 1 The structural schematic diagrams and HSE06 band structures of In_2SSeTe monolayers (a) and (c) for In_2SSeTe-$P_{\downarrow}$, (b) and (d) for In_2SSeTe-$P_{\uparrow}$.

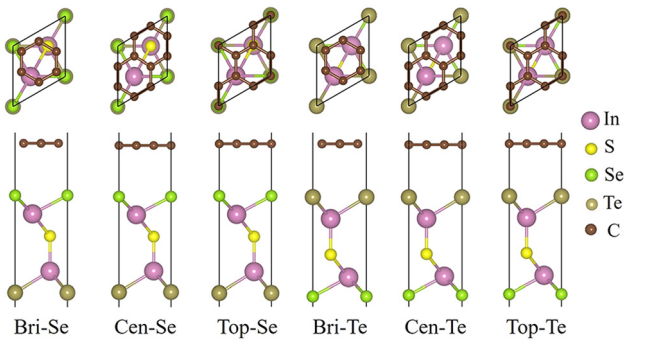

Fig. 2 The schematic diagrams of different stacking configurations for graphene/In_2SSeTe-$P_{\downarrow}$ heterostructures.

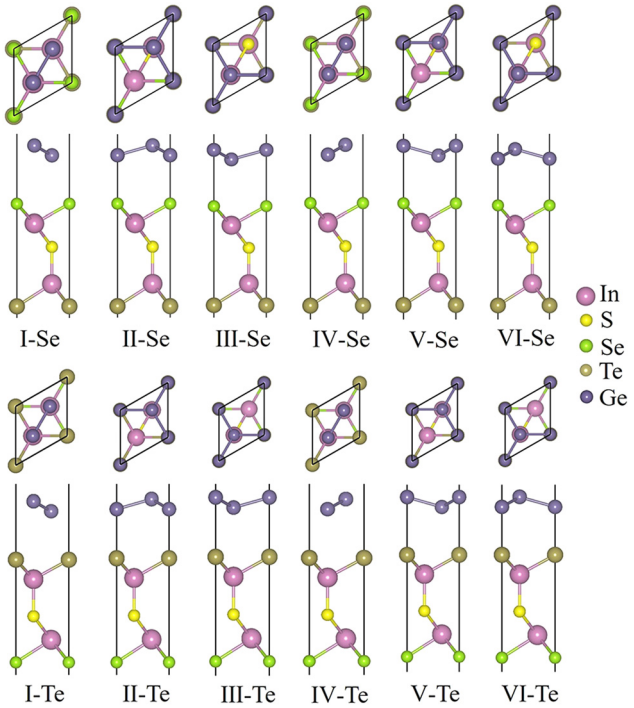

Fig. 3 The schematic diagrams of different stacking configurations for germanene/$In_2SSeTe\text{-}P_\downarrow$ heterostructures.

other hand, since each surface of $In_2SSeTe\text{-}P_\downarrow$ has six different stacking configurations with germanene by shifting and rotating the upper germanene layers, there are twelve different stacking configurations for germanene/$In_2SSeTe\text{-}P_\downarrow$ heterostructures, as shown in Fig. 3. To determine the most stable stacking configurations, the binding energies (E_b) and formation energies (E_f) of the heterostructures are calculated, which are defined as

$$E_b = (E_H^{total} - E_{upper}^{fix} - E_{bottom}^{fix})/S \quad (3)$$

$$E_f = (E_H^{total} - E_{upper} - E_{bottom}) \quad (4)$$

where E_H^{total} represents the total energy of the heterostructure. E_{upper}^{fix} and E_{upper}^{fix} are the total energies of the upper and bottom monolayers constrained in the heterostructure lattice constants, respectively. S is the heterostructure interfacial area. And E_{upper} and E_{bottom} stand for the total energies of the freestanding upper and bottom monolayers, respectively. Tables 1 and 2 list the calculated results for graphene/$In_2SSeTe\text{-}P_\downarrow$ and germanene/$In_2SSeTe\text{-}P_\downarrow$ heterostructures with different stacking configurations, respectively. All the binding energies around -20 meV Å^{-2} reveal that the different monolayers are connected by the long range van der Waals (vdW) force. Comparing the calculated E_b and E_f for graphene/$In_2SSeTe\text{-}P_\downarrow$ and germanene/$In_2SSeTe\text{-}P_\downarrow$ heterostructures, it is deduced that the interlayer binding force of the germanene/$In_2SSeTe\text{-}P_\downarrow$ heterostructure is stronger than that of the graphene/$In_2SSeTe\text{-}P_\downarrow$ heterostructure. In addition, the Se surface of $In_2SSeTe\text{-}P_\downarrow$ is more energetically favorable to absorb on graphene and germanene than the Te surface. The most stable stacking configurations are Cen-Se type for the graphene/$In_2SSeTe\text{-}P_\downarrow$ heterostructure and I-Se type for the germanene/$In_2SSeTe\text{-}P_\downarrow$ heterostructure. As a result, we will focus on these stable configurations in the following analysis.

Table 1 The binding energies (E_b, meV Å^{-2}) and formation energies (E_f, eV) of different stacking configurations for graphene/$In_2SSeTe\text{-}P_\downarrow$ heterostructures

Stacking configuration	E_b-Se	E_b-Te	E_f-Se	E_f-Te
Bridge	−14.995	−14.398	−0.180	−0.171
Center	−15.308	−14.750	−0.186	−0.177
Top	−14.970	−14.359	−0.181	−0.171

Table 2 The binding energies (E_b, meV Å^{-2}) and formation energies (E_f, eV) of different stacking configurations for germanene/$In_2SSeTe\text{-}P_\downarrow$ heterostructures

Stacking configuration	E_b-Se	E_b-Te	E_f-Se	E_f-Te
I	−23.482	−22.413	−0.316	−0.300
II	−18.922	−14.920	−0.243	−0.190
III	−15.454	−15.379	−0.200	−0.197
IV	−22.268	−22.285	−0.299	−0.298
V	−16.062	−15.516	−0.209	−0.199
VI	−17.507	−14.778	−0.223	−0.188

The phase transition energy barriers of the polarization reversal processes are essential for the switching performance of ferroelectric devices.[69,70] The most effective polarization reversal pathway without an electric field connects the two degenerate states with different polarities.[26] Therefore, we calculated the phase transition process of the activation barrier against direct shifting of the central S layer using the climbing-image nudged elastic band (CINEB) method. As shown in Fig. 4, the energy barriers against direct shifting of the central S layer are 0.781, 0.778 and 0.722 eV per unit cell from $In_2SSeTe\text{-}P_\downarrow$ to $In_2SSeTe\text{-}P_\uparrow$, graphene/$In_2SSeTe\text{-}P_\downarrow$ to graphene/$In_2SSeTe\text{-}P_\uparrow$ and germanene/$In_2SSeTe\text{-}P_\downarrow$ to germanene/$In_2SSeTe\text{-}P_\uparrow$, respectively. On the other hand, the energy barriers of reverse processes are 0.782, 0.749 and 0.721 eV per unit cell from $In_2SSeTe\text{-}P_\uparrow$ to $In_2SSeTe\text{-}P_\downarrow$, graphene/$In_2SSeTe\text{-}P_\uparrow$ to graphene/$In_2SSeTe\text{-}P_\downarrow$ and germanene/$In_2SSeTe\text{-}P_\uparrow$ to germanene/$In_2SSeTe\text{-}P_\downarrow$, respectively. The calculated energy barriers of In_2SSeTe are about 0.7–0.8 eV per uc, which are lower than the results of In_2Se_3 (~0.85 eV).[26] Interestingly, it can be deduced that the heterostructures are easier to realize polarization reversal than the In_2SSeTe monolayer.

$In_2SeTe\text{-}P_\downarrow$ and $In_2SeTe\text{-}P_\uparrow$ own different electrical conductivities due to their distinguishable electronic structures, which could be one of the physical origins to realize high TER ratios in the corresponding FTJs. At the same time, the different conducting states of the electrodes of graphene/In_2SSeTe and germanene/In_2SSeTe heterostructures can be another crucial reason for the huge TER ratios of these FTJs. Therefore, we turn our attention to the electronic structures of graphene/In_2SSeTe and germanene/In_2SSeTe heterostructures, and the results using HSE06 and PBE methods are plotted in Fig. 5 and Fig. S3 (ESI†), respectively. For graphene/$In_2SSeTe\text{-}P_\downarrow$ and graphene/$In_2SSeTe\text{-}P_\uparrow$ heterostructures, the projected band structures (PBSs) of graphene, $In_2SSeTe\text{-}P_\downarrow$ and $In_2SSeTe\text{-}P_\uparrow$ show the same shape as the band structures of their isolated

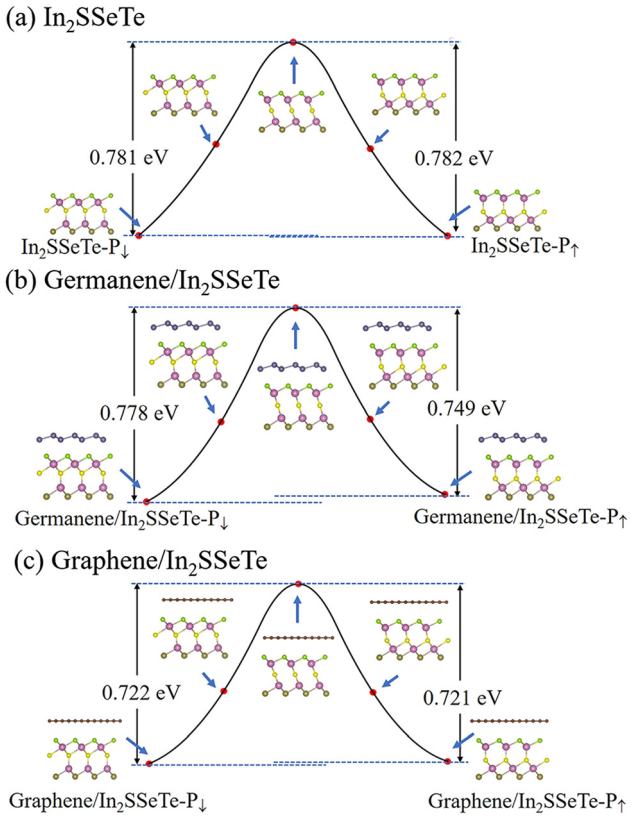

Fig. 4 Kinetics pathways of polarization reversal processes of (a) In_2SSeTe, (b) germanene/In_2SSeTe heterostructures and (c) graphene/In_2SSeTe heterostructures.

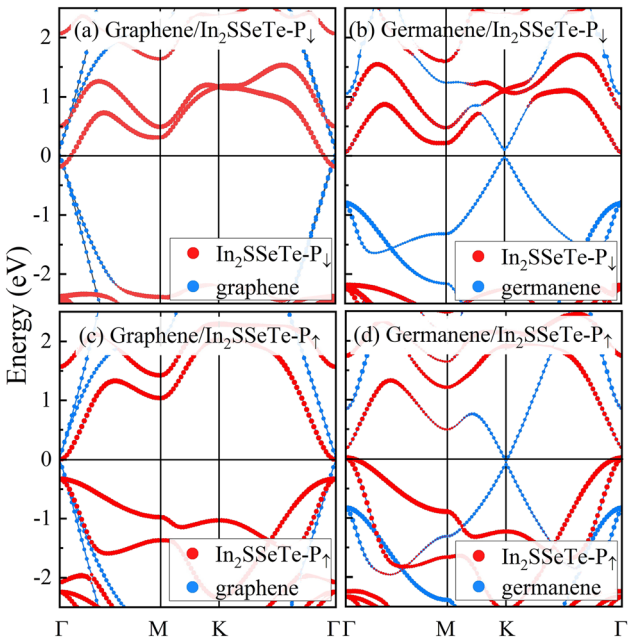

Fig. 5 The projected band structures of (a) graphene/In_2SSeTe-P↓, (b) germanene/In_2SSeTe-P↓, (c) graphene/In_2SSeTe-P↑ and (d) germanene/In_2SSeTe-P↑ heterostructures using the HSE06 method.

monolayers using both methods. It is due to graphene and In_2SSeTe layers connecting with vdW force, which results in little hybridization between these two layers. The PBSs of heterostructures show an upward or downward shift compared with the band structures of the corresponding monolayers. For the PBSs of graphene/In_2SSeTe-P↓ and graphene/In_2SSeTe-P↑ heterostructures shown in Fig. 5(a) and (c), the PBS of graphene moves up with respect to the Fermi level, and that of In_2SSeTe possesses a conversely downward shift. As shown in Fig. 5(b), for germanene/In_2SSeTe-P↓ heterostructures, the PBSs of graphene and In_2SSeTe move upward and downward, respectively. However, the PBSs of germanene and In_2SSeTe for germanene/In_2SSeTe-P↑ heterostructures shown in Fig. 5(d) move downward and upward, respectively, which is converse to that of germanene/In_2SSeTe-P↓ heterostructures. The different band structures for the different heterostructures are mainly determined by the interlayer charge transfers, as shown in Fig. S4 (ESI†). It can be seen that In_2SSeTe layers obtain electrons and graphene/germanene layers lose electrons for graphene/In_2SSeTe-P↓, graphene/In_2SSeTe-P↑ and germanene/In_2SSeTe-P↓ heterostructures, hence the PBSs of In_2SSeTe and graphene or germanene show a downward and upward shift, respectively. Nevertheless, the germanene layer of germanene/In_2SSeTe-P↑ heterostructures obtains electrons and the In_2SSeTe layer loses electrons, resulting in a converse shift of the projected band structures. Besides, it is noted that the PBSs of In_2SSeTe-P↓ for graphene/In_2SSeTe-P↓ and the PBSs of In_2SSeTe-P↑ for graphene/In_2SSeTe-P↑ heterostructures cross the Fermi level, resulting in Ohmic contacts, which can significantly improve the carrier transfer and injection efficiency.[71,72] For germanene/In_2SSeTe heterostructures, the PBSs of In_2SSeTe-P↓ for germanene/In_2SSeTe-P↓ heterostructures are separated by the Fermi level showing Schottky contact, which is not beneficial for the carrier transfer. Moreover, the PBSs of germanene/In_2SSeTe-P↑ heterostructures show Ohmic contact, which is similar to the graphene/In_2SSeTe heterostructures. These results will lead to a more significant difference in conductivity between the P↓ and P↑ states of germanene-based FTJs, indicating that germanene-based FTJs might have a better performance than graphene-based FTJs.

To understand why graphene/In_2SSeTe and germanene/In_2SSeTe heterostructures show different charge transfer natures, we calculated the electrostatic potential of different isolated monolayers, as depicted in Fig. 6. The work function determines the direction of electron transfer when isolated monolayers form heterostructures,[73] as shown in the corresponding figures. For In_2SSeTe-P↓ and In_2SSeTe-P↑, the work functions of the Te surface of W_{Te}-P↓/W_{Te}-P↑ are different from those of the Se surface due to the broken spatial inversion symmetry. The different work functions on two surfaces will result in a built-in electric field ($\Delta\varphi$). The $\Delta\varphi$ of In_2SSeTe with the P↓ state is 1.49 eV, hence the direction of the electric field is from the Te surface to the Se surface. The $\Delta\varphi$ of In_2SSeTe with the P↑ state is 0.90 eV, hence the direction of the electric field is from the Se surface to the Te surface. Besides, the calculated work functions of graphene and germanene are 4.26 eV and

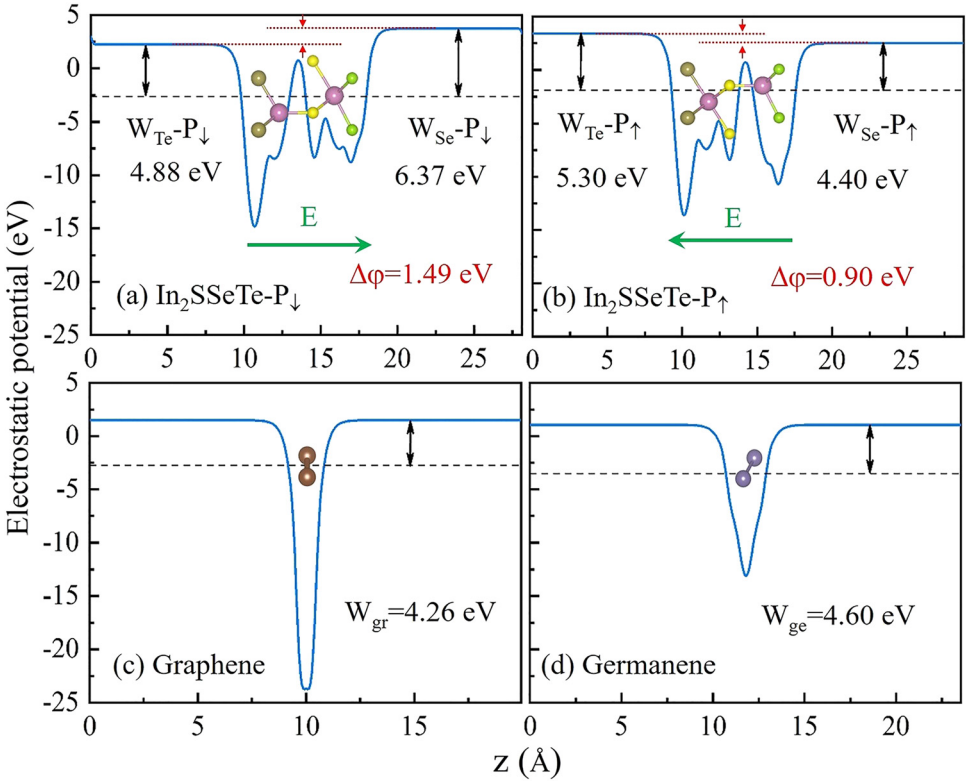

Fig. 6 The electrostatic potential of (a) and (b) monolayered In_2SSeTe with $P_\downarrow$ and $P_\uparrow$, (c) graphene (W_{gr}) and (d) germanene (W_{ge}).

4.60 eV, respectively. When two different two-dimensional materials form a heterostructure, the electrons will flow from the lower work function side to the higher work function side until their Fermi levels are equal.[74] Therefore, the work functions of the Se surface of In_2SSeTe with $P_\downarrow$ and $P_\uparrow$ states are lower than those of graphene and germanene, and the Se surfaces of In_2SSeTe in graphene/In_2SSeTe-$P_\downarrow$, graphene/In_2SSeTe-$P_\uparrow$ and germanene/In_2SSeTe-$P_\downarrow$ heterostructures lose electrons, while graphene/germanene layers gain electrons. Besides, the Se surface of In_2SSeTe in germanene/In_2SSeTe-$P_\uparrow$ heterostructures gains electrons while graphene/germanene layers lose electrons, due to the work function of the Se surface of In_2SSeTe with $P_\uparrow$ states being lower than that of germanene.

By employing graphene/In_2SSeTe and germanene/In_2SSeTe heterostructures as the electrodes and In_2SSeTe monolayer as the central scattering region, the FTJ models with different polarizations of In_2SSeTe ($P_\downarrow$ and $P_\uparrow$) namely Gr-$P_\downarrow$, Gr-$P_\uparrow$, Ge-$P_\downarrow$ and Ge-$P_\uparrow$ FTJs are constructed as shown in Fig. 7. To comprehensively investigate the transport properties *versus* the lengths of the central scattering region in FTJs, we calculated the electronic transport-related behavior of such FTJs with the central scattering region lengths of 5 nm, 7 nm and 9 nm. The zero-bias transmission coefficient curves are shown in Fig. 8. For the transmission coefficient curves of Gr-$P_\downarrow$ FTJs, there is a sharp dip at −1 eV below the Fermi level and a sharp rise near the Fermi level. As a result, the energy region from −1 eV to −0.2 eV has much lower transmission coefficients. For the transmission coefficient curves of Gr-$P_\uparrow$ FTJs, there is a sharp dip at −0.1 eV below the Fermi level, and the transmission coefficient curves dip to a much deeper level with the central scattering region length increasing from 5 nm to 9 nm. On the other hand, there are two small trenches for the transmission coefficient curves of the Ge-$P_\uparrow$ FTJs with different central scattering region lengths located at the Fermi level and around 0.2 eV, respectively. The lowest transmission region of Ge-$P_\downarrow$ FTJs occurred at −0.4 to −0.1 eV, which shows a distinct magnitude difference from the Ge-$P_\uparrow$ FTJs and implies that huge TER ratios will be achieved below the Fermi level. There is a sharp rise around the Fermi level, and the transmission coefficients are almost coincident when the energy is higher than 0.2 eV, indicating a sharp drop of TER ratios.

The zero-bias tunnel electroresistance (TER) ratio curves with the energy region from −1.5 eV to 1.5 eV are shown in Fig. 9. The results of graphene-based and germanene-based FTJs are given in the left and right panels, respectively. It should be noted that the highest TER ratios occurred at around −0.7 eV and −0.4 eV for graphene-based and germanene-based FTJs, respectively. The values of the highest TER ratios increase exponentially with the length of the central scattering region. Table 3 summarizes the calculated transmission coefficients and TER ratios at the Fermi level of the Gr-$P_\downarrow$ ($T_{Gr\text{-}P_\downarrow}$), Gr-$P_\uparrow$ ($T_{Gr\text{-}P_\uparrow}$), Ge-$P_\downarrow$ ($T_{Ge\text{-}P_\downarrow}$) and Ge-$P_\uparrow$ ($T_{Ge\text{-}P_\uparrow}$) FTJs. Herein, the transmission coefficients for the FTJs with $P_\uparrow$ states are much higher than those of the $P_\downarrow$ states, resulting in an apparent TER effect. The best performances are found at the FTJs with 9 nm central scattering region length for both

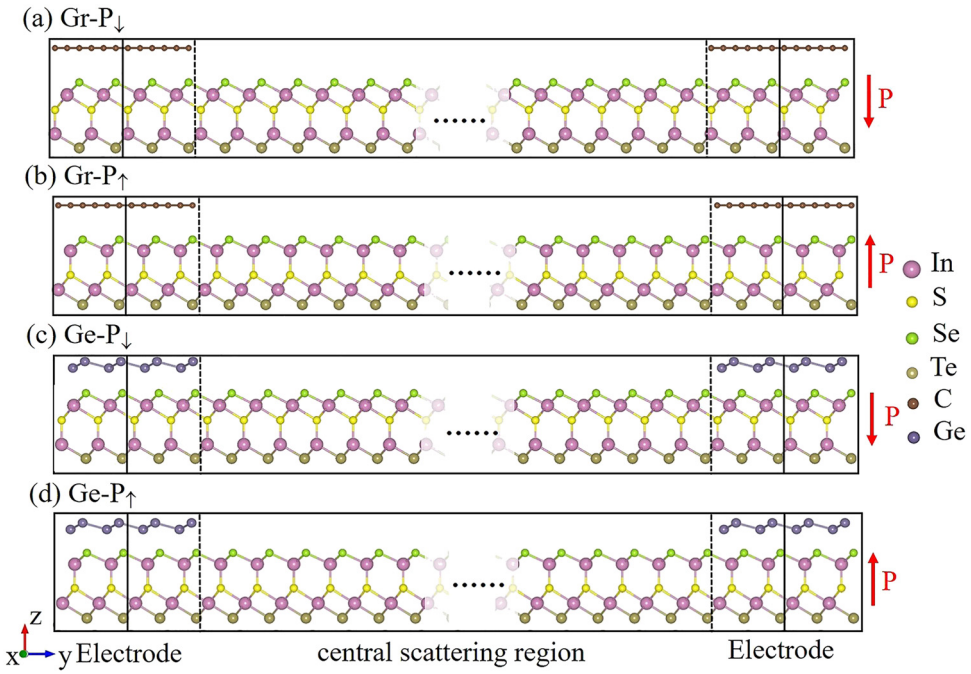

Fig. 7 The schematic diagrams of the FTJs with downward ($P_{\downarrow}$) and upward ($P_{\uparrow}$) polarization. (a) Gr-$P_{\downarrow}$ and (b) Gr-$P_{\uparrow}$ FTJs, for the graphene/In_2SSeTe heterostructure as electrodes. (c) Ge-$P_{\downarrow}$ and (d) Ge-$P_{\uparrow}$ FTJs for the germanene/In_2SSeTe heterostructure as electrodes. The lengths of the central scattering regions are set to 5 nm, 7 nm and 9 nm, respectively.

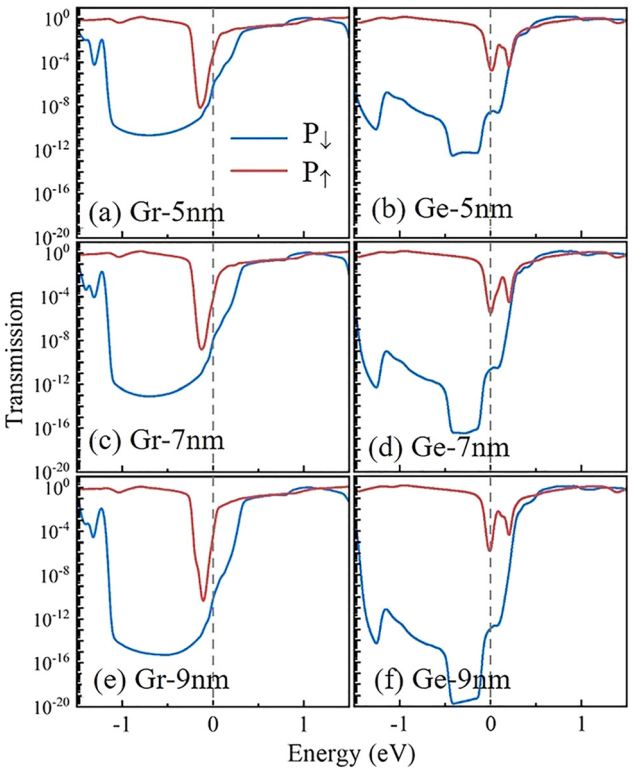

Fig. 8 The zero-bias transmission coefficient curves for (a), (c) and (e) graphene(Gr)-based FTJs, (b), (d) and (f) germanene (Ge)-based FTJs with the central scattering region lengths of 5 nm, 7 nm and 9 nm.

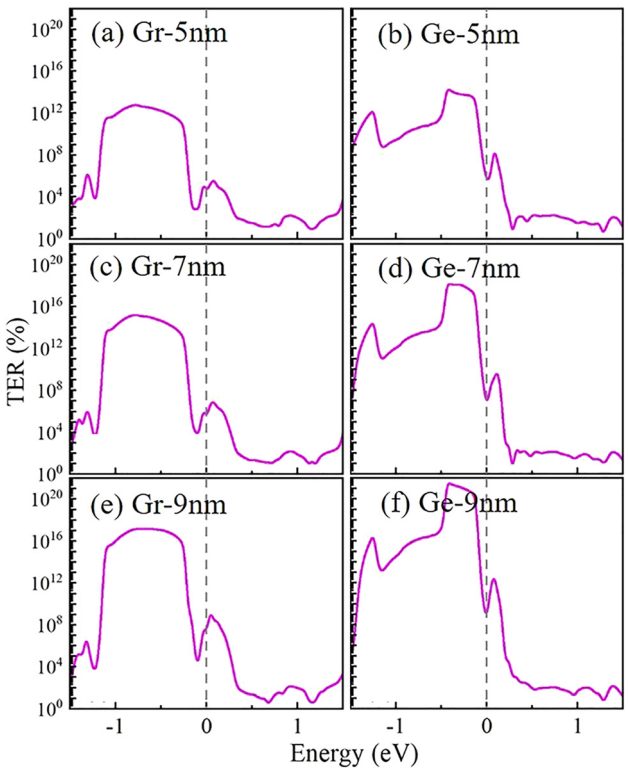

Fig. 9 The zero-bias tunnel electroresistance (TER) ratio curves for (a), (c) and (e) graphene(Gr)-based FTJs; (b), (d) and (f) germanene (Ge)-based FTJs with the central scattering region lengths of 5 nm, 7 nm and 9 nm.

Table 3 The transmission coefficients and TER ratios at the Fermi level for the Gr-$P_\downarrow$ ($T_{Gr\text{-}P_\downarrow}$), Gr-$P_\uparrow$ ($T_{Gr\text{-}P_\uparrow}$), Ge-$P_\downarrow$ ($T_{Ge\text{-}P_\downarrow}$) and Ge-$P_\uparrow$ ($T_{Ge\text{-}P_\uparrow}$) FTJs

Central scattering region length	$T_{Gr\text{-}P_\downarrow}$	$T_{Gr\text{-}P_\uparrow}$	TER ratio	$T_{Ge\text{-}P_\downarrow}$	$T_{Ge\text{-}P_\uparrow}$	TER ratio
5 nm	1.25×10^{-6}	4.06×10^{-4}	3.24×10^{4}%	3.55×10^{-9}	8.63×10^{-6}	2.43×10^{5}%
7 nm	1.88×10^{-8}	4.94×10^{-5}	2.63×10^{5}%	2.54×10^{-11}	6.45×10^{-7}	2.54×10^{6}%
9 nm	1.33×10^{-10}	2.99×10^{-5}	2.24×10^{7}%	1.49×10^{-13}	4.42×10^{-7}	2.98×10^{8}%

graphene-based and germanene-based FTJs due to their huge TER ratios of 2.24×10^{7}% and 2.98×10^{8}%, respectively. Besides, the calculated TER ratios reveal that germanene-based FTJs have better application potential than graphene-based FTJs, regardless of the thickness of the devices, which agrees well with our previous electronic structure analysis.

In order to better understand the behaviors of transmission states and transmission channels, the eigenfunctions of 5 nm, 7 nm and 9 nm FTJs for the Fermi level and $(k_x, k_y) = (0, 0)$ wave vector space were calculated and are plotted in Fig. 10, Fig. S5 and S6 (ESI†), respectively. The transmission channels of the electrons in $P_\uparrow$ and $P_\downarrow$ states are shown as 3D contour plots, the isosurface value is chosen to be 0.02 e.u., which is sufficient to show the contribution of each atom. As shown in Fig. 10(a) and (c), the transmission eigenstates of Gr-$P_\downarrow$ and Ge-$P_\downarrow$ FTJs decay from the left electrode to the right electrode, resulting in electronic states that are only localized at the left part of FTJs. In this case, the electrons cannot pass from the left to the right electrode, and the FTJs are in a high resistance state. As depicted in Fig. 10(b) and (d), the transmission eigenstates of Gr-$P_\uparrow$ and Ge-$P_\uparrow$ FTJs can be found in the whole FTJs, revealing that the electrons can flow effortlessly from the left electrode and right electrode, and this is a typical conductive mode.

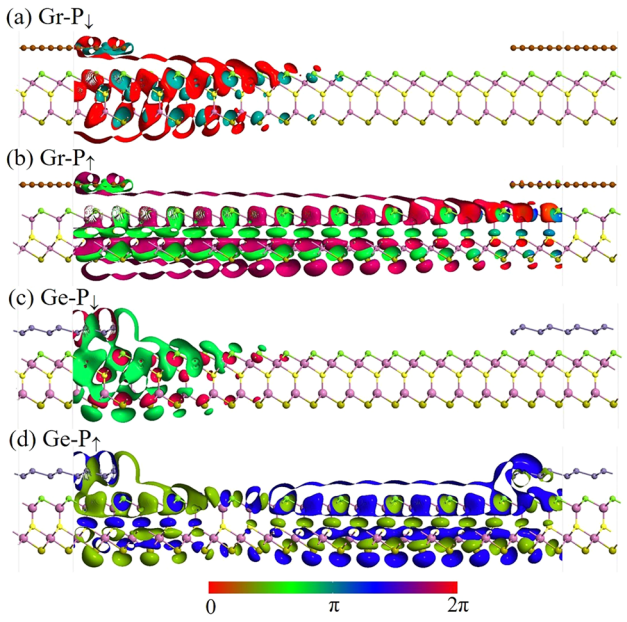

Fig. 10 The contour plot of the transmission eigenstates at the Fermi level and $(k_x, k_y) = (0, 0)$ of (a) Gr-$P_\downarrow$, (b) Gr-$P_\uparrow$, (c) Ge-$P_\downarrow$ and (d) Ge-$P_\uparrow$ FTJs with the central scattering region length of 5 nm. The isosurface value is 0.02 a.u.

Conclusion

In summary, based on density functional theory and the non-equilibrium Green's function method, we systematically studied two types of lateral ferroelectric tunnel junctions (FTJs) by employing Janus monolayer In_2SSeTe as the central scattering region and In_2SSeTe/graphene or In_2SSeTe/germanene as electrodes. The constructed FTJs have different electrical conductivities when In_2SSeTe of the FTJs has $P_\downarrow$ and $P_\uparrow$ states, resulting in an apparent tunneling resistance effect. Except for In_2SSeTe with $P_\downarrow$ and $P_\uparrow$ states of the central scattering regions showing different electrical conductivities due to the difference in monolayer band structures, the different conducting behaviors of In_2SSeTe in the electrode regions can be another crucial reason for the huge TER ratios. Further analysis indicates that the different conducting behaviors of In_2SSeTe in the electrodes arise from the difference in work functions of the two surfaces of In_2SSeTe. To determine the length dependence on the performance of FTJs, we investigated the electronic transport-related behavior of graphene and germanene-based FTJs with 5 nm, 7 nm and 9 nm central scattering region lengths. The results show that the TER ratios of both types of FTJs increased with the increase of the device length, and the maximum TER ratios were 2.24×10^{7}% and 2.98×10^{8}% for graphene and germanene-based FTJs with 9 nm central scattering region length. These results reveal that such FTJs show great potential application in nonvolatile memory devices.

Author contributions

Zhou Cui: Investigation, formal analysis, and writing – original draft. Ting Li: data curation, and validation. Rui Xiong: data curation and validation. Cuilian Wen: visualization, formal analysis, and writing – review & editing. Yinggan Zhang: formal analysis and writing – review & editing. Jingying Zheng: formal analysis and writing – review & editing. Bo Wu: writing – review & editing. Baisheng Sa: project administration, supervision, and writing –review & editing.

Conflicts of interest

The authors declare no competing financial interest.

Acknowledgements

This work was supported by the National Key Research and Development Program of China (No. 2022YFB3807200), the National Natural Science Foundation of China (No. 21973012, 21905050 and 52201022), the Natural Science Foundation of

Fujian Province (No. 2021J06011, 2020J01351, 2020J01474, 2021H6011 and 2021J01590), and the ''Qishan Scholar'' Scientific Research Project of Fuzhou University.

References

1 C. R. Bowen, H. A. Kim, P. M. Weaver and S. Dunn, Piezoelectric and ferroelectric materials and structures for energy harvesting applications, *Energy Environ. Sci.*, 2014, **7**, 25–44.
2 L. W. Martin and A. M. Rappe, Thin-film ferroelectric materials and their applications, *Nat. Rev. Mater.*, 2016, **2**, 1–14.
3 M. Wu, S. Dong, K. Yao, J. Liu and X. C. Zeng, Ferroelectricity in Covalently functionalized Two-dimensional Materials: Integration of High-mobility Semiconductors and Nonvolatile Memory, *Nano Lett.*, 2016, **16**, 7309–7315.
4 Q. Yang, T. Zhong, Z. Tu, L. Zhu, M. Wu and X. C. Zeng, Design of Single-Molecule Multiferroics for Efficient Ultrahigh-Density Nonvolatile Memories, *Adv. Sci.*, 2019, **6**, 1801572.
5 A. Gruverman, D. Wu, H. Lu, Y. Wang, H. W. Jang, C. M. Folkman, M. Y. Zhuravlev, D. Felker, M. Rzchowski, C. B. Eom and E. Y. Tsymbal, Tunneling electroresistance effect in ferroelectric tunnel junctions at the nanoscale, *Nano Lett.*, 2009, **9**, 3539–3543.
6 R. Soni, A. Petraru, P. Meuffels, O. Vavra, M. Ziegler, S. K. Kim, D. S. Jeong, N. A. Pertsev and H. Kohlstedt, Giant electrode effect on tunnelling electroresistance in ferroelectric tunnel junctions, *Nat. Commun.*, 2014, **5**, 5414.
7 X. K. Duan, H. Wang, X. F. Chen and J. S. Qi, Multiple polarization phases and strong magnetoelectric coupling in the layered transition metal phosphorus chalcogenides TMP_2X_6(T = Cu, Ag; M = Cr, V; X = S, Se) by controlling the interlayer interaction and dimension, *Phys. Rev. B*, 2022, **106**, 115403.
8 F. Fan, B. Luo, M. Duan, H. Xing, K. Jin and C. Chen, Ferroelectric domain switching investigation of $BiFeO_3$ thin film on Pt/Ti/SiO_2/Si (111) substrate, *Appl. Surf. Sci.*, 2012, **258**, 7412–7416.
9 Q. Pan, Z. B. Liu, Y. Y. Tang, P. F. Li, R. W. Ma, R. Y. Wei, Y. Zhang, Y. M. You, H. Y. Ye and R. G. Xiong, A Three-Dimensional Molecular Perovskite Ferroelectric: (3-Ammoniopyrrolidinium)$RbBr_3$, *J. Am. Chem. Soc.*, 2017, **139**, 3954–3957.
10 L. L. Tao and J. Wang, Ferroelectricity and tunneling electroresistance effect driven by asymmetric polar interfaces in all-oxide ferroelectric tunnel junctions, *Appl. Phys. Lett.*, 2016, **108**, 062903.
11 V. S. Borisov, S. Ostanin, S. Achilles, J. Henk and I. Mertig, Spin-dependent transport in a multiferroic tunnel junction: Theory for Co/$PbTiO_3$/Co, *Phys. Rev. B: Condens. Matter Mater. Phys.*, 2015, **92**, 075137.
12 C. Li, L. Huang, T. Li, W. Lu, X. Qiu, Z. Huang, Z. Liu, S. Zeng, R. Guo, Y. Zhao, K. Zeng, M. Coey, J. Chen, Ariando and T. Venkatesan, Ultrathin $BaTiO_3$-based ferroelectric tunnel junctions through interface engineering, *Nano Lett.*, 2015, **15**, 2568–2573.
13 W. Xiao, L. Kang, H. Hao, Y. Zhou, X. Zheng, L. Zhang and Z. Zeng, Giant Tunneling Electroresistance Induced by Interfacial Doping in Pt/$BaTiO_3$/Pt Ferroelectric Tunnel Junctions, *Phys. Rev. A: At., Mol., Opt. Phys.*, 2022, **17**, 044001.
14 Z. Xi, J. Ruan, C. Li, C. Zheng, Z. Wen, J. Dai, A. Li and D. Wu, Giant tunnelling electroresistance in metal/ferroelectric/semiconductor tunnel junctions by engineering the Schottky barrier, *Nat. Commun.*, 2017, **8**, 15217.
15 D. D. Fong, G. B. Stephenson, S. K. Streiffer, J. A. Eastman, O. Auciello, P. H. Fuoss and C. Thompson, Ferroelectricity in ultrathin perovskite films, *Science*, 2004, **304**, 1650.
16 M. Trieloff, E. K. Jessberger, I. Herrwerth, J. Hopp, C. Fieni, M. Ghelis, M. Bourot-Denise and P. Pellas, Structure and thermal history of the H-chondrite parent asteroid revealed by thermochronometry, *Nature*, 2003, **422**, 506.
17 Y. S. Kim, D. H. Kim, J. D. Kim, Y. J. Chang, T. W. Noh, J. H. Kong, K. Char, Y. D. Park, S. D. Bu, J. G. Yoon and J. S. Chung, Critical thickness of ultrathin ferroelectric $BaTiO_3$ films, *Appl. Phys. Lett.*, 2005, **86**, 102907.
18 M. Stengel and N. A. Spaldin, Origin of the dielectric dead layer in nanoscale capacitors, *Nature*, 2006, **443**, 679–682.
19 K. S. Novoselov, A. K. Geim, S. V. Morozov, D. Jiang, Y. Zhang, S. V. Dubonos, I. V. Grigorieva and A. A. Firsov, Electric Field Effect in Atomically Thin Carbon Films, *Science*, 2004, **306**, 666–669.
20 D. S. Schulman, A. J. Arnold and S. Das, Contact engineering for 2D materials and devices, *Chem. Soc. Rev.*, 2018, **47**, 3037–3058.
21 R. F. Li, X. J. Yu, C. L. Wen, Y. G. Zhang, H. L. Lin and B. S. Sa, Unexpected Carrier Mobility Anisotropy in the Two-dimensional Ca_2Si Monolayer from First-principles Calculations, *Chin. J. Struct. Chem.*, 2020, **39**, 1243–1251.
22 X. Wang, J. Xu, J. Si, B. Wang and W. Yin, Semiconductor-metal transition caused by increased surface charge in two-dimensional quintuple-layers Al_2O_3 materials, *Appl. Surf. Sci.*, 2023, **610**, 155614.
23 A. Belianinov, Q. He, A. Dziaugys, P. Maksymovych, E. Eliseev, A. Borisevich, A. Morozovska, J. Banys, Y. Vysochanskii and S. V. Kalinin, $CuInP_2S_6$ Room Temperature Layered Ferroelectric, *Nano Lett.*, 2015, **15**, 3808–3814.
24 F. Liu, L. You, K. L. Seyler, X. Li, P. Yu, J. Lin, X. Wang, J. Zhou, H. Wang, H. He, S. T. Pantelides, W. Zhou, P. Sharma, X. Xu, P. M. Ajayan, J. Wang and Z. Liu, Room-temperature ferroelectricity in $CuInP_2S_6$ ultrathin flakes, *Nat. Commun.*, 2016, **7**, 12357.
25 M. Chyasnavichyus, M. A. Susner, A. V. Ievlev, E. A. Eliseev, S. V. Kalinin, N. Balke, A. N. Morozovska, M. A. McGuire and P. Maksymovych, Size-effect in layered ferrielectric $CuInP_2S_6$, *Appl. Phys. Lett.*, 2016, **109**, 172901.
26 W. Ding, J. Zhu, Z. Wang, Y. Gao, D. Xiao, Y. Gu, Z. Zhang and W. Zhu, Prediction of intrinsic two-dimensional ferroelectrics in In_2Se_3 and other III2-VI3 van der Waals materials, *Nat. Commun.*, 2017, **8**, 14956.
27 Y. Zhou, D. Wu, Y. Zhu, Y. Cho, Q. He, X. Yang, K. Herrera, Z. Chu, Y. Han, M. C. Downer, H. Peng and K. Lai, Out-of-Plane Piezoelectricity and Ferroelectricity in Layered alpha-In_2Se_3 Nanoflakes, *Nano Lett.*, 2017, **17**, 5508–5513.

28 R. Fei, W. Kang and L. Yang, Ferroelectricity and Phase Transitions in Monolayer Group-IV Monochalcogenides, *Phys. Rev. Lett.*, 2016, **117**, 097601.
29 H. Wang and X. Qian, Giant Optical Second Harmonic Generation in Two-Dimensional Multiferroics, *Nano Lett.*, 2017, **17**, 5027–5034.
30 L. Qi, S. Ruan and Y. J. Zeng, Review on Recent Developments in 2D Ferroelectrics: Theories and Applications, *Adv. Mater.*, 2021, **33**, e2005098.
31 X. W. Shen, Y. W. Fang, B. B. Tian and C. G. Duan, Two-Dimensional Ferroelectric Tunnel Junction: The Case of Monolayer In:SnSe/SnSe/Sb:SnSe Homostructure, *ACS Appl. Electron. Mater.*, 2019, **1**, 1133–1140.
32 L. Kang, P. Jiang, H. Hao, Y. Zhou, X. Zheng, L. Zhang and Z. Zeng, Giant tunnel electroresistance in ferroelectric tunnel junctions with metal contacts to two-dimensional ferroelectric materials, *Phys. Rev. B*, 2021, **103**, 125414.
33 L. Kang, P. Jiang, H. Hao, Y. Zhou, X. Zheng, L. Zhang and Z. Zeng, Giant tunneling electroresistance in two-dimensional ferroelectric tunnel junctions with out-of-plane ferroelectric polarization, *Phys. Rev. B*, 2020, **101**, 014105.
34 R. Li, Y. Cheng and W. Huang, Recent Progress of Janus 2D Transition Metal Chalcogenides: From Theory to Experiments, *Small*, 2018, **14**, e1802091.
35 Z. Zhou, X. Niu, Y. Zhang and J. Wang, Janus MoSSe/WSeTe heterostructures: a direct Z-scheme photocatalyst for hydrogen evolution, *J. Mater. Chem. A*, 2019, **7**, 21835–21842.
36 L. Dong, J. Lou and V. B. Shenoy, Large In-Plane and Vertical Piezoelectricity in Janus Transition Metal Dichalchogenides, *ACS Nano*, 2017, **11**, 8242–8248.
37 P. Wang, H. Liu, Y. Zong, H. Wen, J. B. Xia and H. B. Wu, Two-Dimensional In_2X_2X' (X and X' = S, Se, and Te) Monolayers with an Intrinsic Electric Field for High-Performance Photocatalytic and Piezoelectric Applications, *ACS Appl. Mater. Interfaces*, 2021, **13**, 34178–34187.
38 C. Cui, F. Xue, W. Hu and L. Li, Two-dimensional materials with piezoelectric and ferroelectric functionalities, *npj 2D Mater. Appl.*, 2018, **2**, 1–14.
39 B. Hunt, J. D. Sanchez-Yamagishi, A. F. Young, M. Yankowitz, B. J. LeRoy, K. Watanabe, T. Taniguchi, P. Moon, M. Koshino, P. Jarillo-Herrero and R. C. Ashoori, Massive Dirac fermions and Hofstadter butterfly in a van der Waals heterostructure, *Science*, 2013, **340**, 1427–1430.
40 L. A. Ponomarenko, R. V. Gorbachev, G. L. Yu, D. C. Elias, R. Jalil, A. A. Patel, A. Mishchenko, A. S. Mayorov, C. R. Woods, J. R. Wallbank, M. Mucha-Kruczynski, B. A. Piot, M. Potemski, I. V. Grigorieva, K. S. Novoselov, F. Guinea, V. I. Fal'ko and A. K. Geim, Cloning of Dirac fermions in graphene superlattices, *Nature*, 2013, **497**, 594–597.
41 Z. Wang, Q. Chen and J. Wang, Electronic Structure of Twisted Bilayers of Graphene/MoS_2 and MoS_2/MoS_2, *J. Phys. Chem. C*, 2015, **119**, 4752–4758.
42 X. Yang, B. Sa, P. Lin, C. Xu, Q. Zhu, H. Zhan and Z. Sun, Tunable Contacts in Graphene/InSe van der Waals Heterostructures, *J. Phys. Chem. C*, 2020, **124**, 23699–23706.
43 Z. Zhu, X. Chen, W. Li and J. Qi, Electric field control of the semiconductor-metal transition in two dimensional $CuInP_2S_6$/germanene van der Waals heterostructure, *Appl. Phys. Lett.*, 2019, **114**, 223102.
44 R. Xiong, W. Li, Y. Zhang, Z. Cui, C. Wen, M. Anpo, B. Wu and B. Sa, Computational discovery of In_2XY_2 (X, Y = S, Se, and Te; X ≠ Y) monolayers as multifunctional energy conversion materials, *J. Mater. Chem. C*, 2022, **10**, 10480–10490.
45 G. Wang, K. Li, L. Peng, Y. Zhang, J. Zhou and Z. Sun, High-Throughput Automatic Integrated Material Calculations and Data Management Intelligent Platform and the Application in Novel Alloys, *Acta Metall. Sinica*, 2022, **58**, 75–88.
46 G. Wang, L. Peng, K. Li, L. Zhu, J. Zhou, N. Miao and Z. Sun, ALKEMIE: An intelligent computational platform for accelerating materials discovery and design, *Comput. Mater. Sci.*, 2021, **186**, 110064.
47 G. Kresse and J. Furthmüller, Efficient iterative schemes for ab initio total-energy calculations using a plane-wave basis set, *Phys. Rev. B: Condens. Matter Mater. Phys.*, 1996, **54**, 11169.
48 J. P. Perdew, K. Burke and M. Ernzerhof, Generalized Gradient Approximation Made Simple, *Phys. Rev. Lett.*, 1996, **77**, 3865.
49 S. Grimme, J. Antony, S. Ehrlich and H. Krieg, A consistent and accurate ab initio parametrization of density functional dispersion correction (DFT-D) for the 94 elements H-Pu, *J. Chem. Phys.*, 2010, **132**, 154104.
50 S. Grimme, S. Ehrlich and L. Goerigk, Effect of the damping function in dispersion corrected density functional theory, *J. Comput. Chem.*, 2011, **32**, 1456–1465.
51 X. Gonze and C. Lee, Dynamical matrices, Born effective charges, dielectric permittivity tensors, and interatomic force constants from density-functional perturbation theory, *Phys. Rev. B: Condens. Matter Mater. Phys.*, 1997, **55**, 10355.
52 S. Nosé, A unified formulation of the constant temperature molecular dynamics methods, *J. Chem. Phys.*, 1984, **81**, 511–519.
53 W. G. Hoover, Canonical dynamics: Equilibrium phase-space distributions, *Phys. Rev. A: At., Mol., Opt. Phys.*, 1985, **31**, 1695–1697.
54 L. Bengtsson, Dipole correction for surface supercell calculations, *Phys. Rev. B: Condens. Matter Mater. Phys.*, 1999, **59**, 12301–12304.
55 J. Heyd, G. E. Scuseria and M. Ernzerhof, Hybrid functionals based on a screened Coulomb potential, *J. Chem. Phys.*, 2003, **118**, 8207–8215.
56 D. Sheppard, R. Terrell and G. Henkelman, Optimization methods for finding minimum energy paths, *J. Chem. Phys.*, 2008, **128**, 134106.
57 G. Henkelman and H. Jónsson, Improved tangent estimate in the nudged elastic band method for finding minimum energy paths and saddle points, *J. Chem. Phys.*, 2000, **113**, 9978–9985.
58 M. Brandbyge, J. L. Mozos, P. Ordejón, J. Taylor and K. Stokbro, Density-functional method for nonequilibrium electron transport, *Phys. Rev. B: Condens. Matter Mater. Phys.*, 2002, **65**, 165401.

59 S. Smidstrup, T. Markussen, P. Vancraeyveld, J. Wellendorff, J. Schneider, T. Gunst, B. Verstichel, D. Stradi, P. A. Khomyakov, U. G. Vej-Hansen, M. E. Lee, S. T. Chill, F. Rasmussen, G. Penazzi, F. Corsetti, A. Ojanpera, K. Jensen, M. L. N. Palsgaard, U. Martinez, A. Blom, M. Brandbyge and K. Stokbro, QuantumATK: an integrated platform of electronic and atomic-scale modelling tools, *J. Phys.: Condens. Matter*, 2020, **32**, 015901.

60 M. J. van Setten, M. Giantomassi, E. Bousquet, M. J. Verstraete, D. R. Hamann, X. Gonze and G. M. Rignanese, The PseudoDojo: Training and grading a 85 element optimized norm-conserving pseudopotential table, *Comput. Phys. Commun.*, 2018, **226**, 39–54.

61 V. Blum, R. Gehrke, F. Hanke, P. Havu, V. Havu, X. Ren, K. Reuter and M. Scheffler, Ab initio molecular simulations with numeric atom-centered orbitals, *Comput. Phys. Commun.*, 2009, **180**, 2175–2196.

62 R. Landauer, Electrical resistance of disordered one-dimensional lattices, *Philos. Mag.*, 2006, **21**, 863–867.

63 J. P. Velev, C. G. Duan, J. Burton, A. Smogunov, M. K. Niranjan, E. Tosatti, S. Jaswal and E. Y. Tsymbal, Magnetic tunnel junctions with ferroelectric barriers: prediction of four resistance states from first principles, *Nano Lett.*, 2009, **9**, 427–432.

64 A. J. Mannix, X. F. Zhou, B. Kiraly, J. D. Wood, D. Alducin, B. D. Myers, X. Liu, B. L. Fisher, U. Santiago, J. R. Guest, M. J. Yacaman, A. Ponce, A. R. Oganov, M. C. Hersam and N. P. Guisinger, Synthesis of borophenes: Anisotropic, two-dimensional boron polymorphs, *Science*, 2015, **350**, 1513–1516.

65 E. S. Penev, A. Kutana and B. I. Yakobson, Can Two-Dimensional Boron Superconduct?, *Nano Lett.*, 2016, **16**, 2522–2526.

66 N. Miao, B. Xu, N. C. Bristowe, J. Zhou and Z. Sun, Tunable Magnetism and Extraordinary Sunlight Absorbance in Indium Triphosphide Monolayer, *J. Am. Chem. Soc.*, 2017, **139**, 11125–11131.

67 J. Ding, D. F. Shao, M. Li, L. W. Wen and E. Y. Tsymbal, Two-Dimensional Antiferroelectric Tunnel Junction, *Phys. Rev. Lett.*, 2021, **126**, 057601.

68 B. Sa and Z. Sun, Electron interactions and Dirac fermions in graphene-$Ge_2Sb_2Te_5$ superlattices, *J. Appl. Phys.*, 2014, **115**, 233714.

69 Z. Wen and D. Wu, Ferroelectric Tunnel Junctions: Modulations on the Potential Barrier, *Adv. Mater.*, 2020, **32**, e1904123.

70 Y. Q. Li, X. Y. Wang, S. Y. Zhu, D. S. Tang, Q. W. He and X. C. Wang, Enhanced vertical polarization and ultra-low polarization switching barriers of two-dimensional SnS/SnSSe ferroelectric heterostructures, *J. Mater. Chem. C*, 2022, **10**, 12132–12140.

71 Y. Shu, K. He, R. Xiong, Z. Cui, X. Yang, C. Xu, J. Zheng, C. Wen, B. Wu and B. Sa, Strain engineering on the electronic properties and interface contact of graphene/GeN_3 van der Waals heterostructure, *Appl. Surf. Sci.*, 2022, **604**, 154540.

72 D. G. Popescu, M. A. Husanu, C. Chirila, L. Pintilie and C. M. Teodorescu, The interplay of work function and polarization state at the Schottky barriers height for Cu/$BaTiO_3$ interface, *Appl. Surf. Sci.*, 2020, **502**, 144101.

73 J. Kang, W. Liu, D. Sarkar, D. Jena and K. Banerjee, Computational Study of Metal Contacts to Monolayer Transition-Metal Dichalcogenide Semiconductors, *Phys. Rev. X*, 2014, **4**, 031005.

74 M. K. Mohanta and A. De, Sarkar, Giant tunability in electrical contacts and doping via inconsiderable normal electric field strength or gating for a high-performance in ultrathin field effect transistors based on 2D BX/graphene (X = P, As) van der Waals heterobilayer, *Appl. Surf. Sci.*, 2020, **526**, 146749.